ROYAL SOCIETY OF CHEMISTRY

Check for updates

Crystal growth of calcium oxalate mono- and dihydrate under laminar flow in microfluidic devices†

Fatma İbiş-Özdemir,[a] René Smeets,[a] Jiali Wang,[a] Priya Dhand,[a] Majid Mohamedhoesein,[a] Frederico Marques Penha, [iD][b] Johan Grievink,[a] Antoine E. D. M. van der Heijden,[a] Herman J. M. Kramer[a] and Huseyin Burak Eral [iD] *[ac]

Calcium oxalate (CaOx) crystallization under laminar flow conditions, relevant for kidney stone formation, was studied in a microfluidic device simulating the geometry of kidney collecting ducts. In a typical microfluidic experiment, two reactive solutions with designated concentrations of calcium (Ca) and oxalate (Ox) ions were brought into contact in a microfluidic channel to create a laminar co-current flow of the two streams. As the streams flow co-currently in the channel, diffusion takes place between the two streams across the channel width, resulting in reactive crystallization leading to CaOx nucleation and growth of CaOx crystals along the mixing front. We studied the growth of these crystals in artificial urine as a function of the fluid flow rate in the channel, the molar ratio of Ca : Ox in the medium and the presence of an organic protein, osteopontin (OPN), known to inhibit the growth of CaOx crystals. Three different flow velocities at a fixed molar ratio of Ca : Ox = 7.5 and four molar ratios of Ca : Ox at a fixed mean flow velocity of 0.035 m s^{-1} were tested. Lastly, three additive OPN concentrations were evaluated: 2.4×10^{-8} mol m^{-3}, 6×10^{-8} mol m^{-3} and 8.4×10^{-8} mol m^{-3}. The mean flow velocity did not alter the crystal growth of CaOx in the studied range, whereas altering the molar ratio of Ca : Ox had a high impact on the growth rate. In addition, the type of pseudopolymorph which nucleated appears to depend strongly on the molar ratio. At a low Ca : Ox ratio, both calcium oxalate monohydrate (COM) and calcium oxalate dihydrate (COD) nucleated simultaneously and the growth of the two pseudopolymorphic forms of CaOx crystals was observed. The lowest applied OPN concentration decreased the growth rate of COD, while higher concentrations of OPN slowed down the nucleation kinetics to a point that it completely inhibited the formation of any CaOx crystal in artificial urine within the investigated timeframe. COD was seen under all the conditions investigated, whilst COM was seen in experiments for Ca : Ox molar ratio values between 5 and 6. Our results were rationalized using finite element simulations supported by solution chemistry modelling.

1. Introduction

Kidney stones are a serious health problem affecting around 12% of the world's population.[1–4] Each human kidney has approximately 1.2 million nephrons comprised of hollow tubes assembled into a single cell layer. It is the smallest structural and functional unit of this organ. The nephrons comprise a renal corpuscle, proximal tubule, loop of Henle, distal tubule, and collecting duct system.[5–7] Around ten nephrons give birth to one single collecting duct whose diameter is about 100 μm.[8,9] The urine flow rate is roughly 10.0 nl min^{-1}, showing laminar flow inside such a collecting duct.[8,10] Overall, the urinary system filters around 150–180 L per day fluid from renal blood flow to keep essential compounds in the blood while removing toxins, ions, and metabolic waste products. Per day, 1.5 liters of urine are extracted after absorbing water through diffusion and active transport.[11,12] If during this extraction process in the kidney, the solution reaches supersaturated conditions for certain

[a] Complex Fluid Processing, Process & Energy Department, Delft University of Technology, Leeghwaterstraat 39, 2628 CB Delft, The Netherlands. E-mail: H.B.Eral@tudelft.nl

[b] Department of Chemical Engineering, KTH Royal Institute of Technology, Teknikringen 42, SE100-44 Stockholm, Sweden

[c] Van't Hoff Laboratory for Physical and Colloid Chemistry, Debye Institute for Nanomaterials Science Utrecht University, 3584 CH Utrecht, The Netherlands

† Electronic supplementary information (ESI) available. See DOI: https://doi.org/10.1039/d4ce01038h

minerals, crystallization of so-called kidney stones can occur. A plethora of physicochemical phenomena such as nucleation, crystal growth, aggregation and adhesion play a role in forming such kidney stones, making their formation a challenging multiscale process to understand.[2–4,11,12]

Approximately 80% of kidney stones are comprised of calcium oxalate (CaOx).[13–15] CaOx occurs in nature as monohydrate (whewellite, $CaC_2O_4 \cdot H_2O$, COM), dihydrate (weddellite, $CaC_2O_4 \cdot 2H_2O$, COD) and trihydrate (caoxite, $CaC_2O_4 \cdot 3H_2O$, COT), differing by the amount of H_2O in their crystalline structure.[16–18] Different hydrated forms are also known as pseudopolymorphs which is a type of polymorphism and characterized by solvate compounds. Calcium oxalate monohydrate (COM) is the most common and stable form with very low water solubility; 1.24×10^{-4} M in ultrapure water at 37 °C.[16,19–21] Kidney stones occur when the urine volume is low, and calcium, salt, oxalate, and urate concentrations are high.[22]

Research has been done on the formation of CaOx in a large variety of solutions ranging from pure calcium and oxalate to complex solutions that mimic the kidney's solutions. These studies showed that numerous compounds may either promote or inhibit the production of stones. Various inorganic and organic compounds such as citrate, magnesium, nephrocalcin, urine prothrombin fragment-1, and osteopontin (OPN) are thought to inhibit stone formation.[23] OPN is a single-chain protein with a molecular weight of roughly 33 kDa, present in urine in amounts greater than 100 nM.[24] Studies show that OPN hinders crystal formation and alters the shape of CaOx crystals.[1,24–26]

In vitro studies focusing on CaOx stone formation in water or artificial urine with different additives have been extensively reported.[27–35] Researchers have examined the effect of the molar ratio,[28] potential inhibitors,[27,31,36] and quality of water on kidney stone formation.[30] To control momentum, heat and mass transfer on the micro-scale, microfluidic approaches have been proposed and successfully implemented for kidney stone formation.[21,37–39] We report on the growth of calcium oxalate (CaOx) crystals in a microchannel, mimicking the geometry of kidney collecting ducts under flow conditions relevant for kidney stone formation. In this device, two solutions carrying Ca^{2+} and Ox^{2-} ions, respectively, are brought into contact with each other in the microchannel and time-lapse images of the emerging crystals are analyzed to determine the type of pseudopolymorph that nucleated and to quantify the average growth rates of the formed crystals. The growth rate of the nucleated COM or COD crystals in artificial urine was studied as a function of the fluid flow rate in the channel, the molar ratio of Ca : Ox, and the inhibitor concentration. To qualitatively rationalize the crystals growing in microfluidic devices, the velocity and the concentration of a diffusing species under laminar flow in the microchannel were calculated *via* COMSOL Multiphysics. The values from COMSOL were used in solution chemistry modelling using Joint Expert Speciation System (JESS) software to find supersaturation values (see details in the ESI†).

2. Materials and methods

2.1. Microfluidic device

A microfluidic device, fabricated with polydimethylsiloxane (PDMS, $(C_2H_6OSi)_n$, The Dow Chemical Company), is used to mimic the collecting duct in a nephron. The microchannel has a length of 1500 μm, a depth of 45 μm and a width of 295 μm.

A mixture of PDMS and curing agents at a 7 : 1 (w/w) ratio is arranged to prepare the chips. The mixture is stirred manually until it is filled with air bubbles and becomes cloudy. Upon mixing, the mixture is centrifuged (Universal 320 R, Hettich Zentrifugen) at 7400 rpm and 20 °C for 15 minutes to remove air bubbles. Then, the transparent PDMS mixture is put onto a silicon wafer (Fig. S1 in the ESI†) produced by lithography in a cleanroom, previously hydrophobized with a thin layer of trichloro(1*H*,1*H*,2*H*,2*H*-perfluorooctyl)silane (Sigma-Aldrich, CAS 78560-45-9) to make the peeling process easier. The silicon wafer is put upside down in a desiccator with 10 μl of trichlorosilane and connected to a vacuum pump. The pressure is lowered to 100 mbar and kept for two hours. After this process, the trichlorosilane-coated silicon wafer can be used four times; then, the hydrophobization protocol needs to be repeated to use the wafer again. The wafer filled with the PDMS mixture is later placed in a desiccator connected to a vacuum pump for 1 hour to eliminate the air bubbles created during the pouring step. The wafer is placed in a 65 °C oven overnight to ensure that the PDMS is completely cured.

Spin coating (Polos 300, The Netherlands) is used to make a closed microfluidic system. A 0.5 ml aliquot of a mixture of PDMS and curing agent at a 10 : 1 ratio is poured onto a glass slide (VWR International), and the glass slide is fully covered with a thin layer of PDMS at 4500 rpm for one minute. The spin-coated glass slide is placed in a 90 °C oven for 20 minutes. The solid PDMS is bonded to a glass slide to make a closed microfluidic device. This device is left in the oven at 65 °C overnight to cure thoroughly. Three holes are punched in the PDMS chip after the curing step is completed: two for inlets and one for an outlet. The resulting microfluidic device is displayed in Fig. S1 in the ESI.†

2.2. Experimental set-up

In the microfluidic device, the growth of CaOx crystals was induced by sending in two inlets calcium chloride ($CaCl_2$) and sodium oxalate ($Na_2C_2O_4$) aqueous solutions in artificial urine, respectively, (see subsection 1.2.5.). The reservoirs with filtered (0.45 μm filter) $CaCl_2$ and $Na_2C_2O_4$ aqueous solutions were connected to a pressure pump (Fluigent, MFCS- EZ) and the microfluidic device with capillary tubing (Warner Instruments, 0.28 mm inner diameter) (Fig. 1a). The volumetric flow rate resulting from a fixed applied pressure used in this study was measured by weighing the amount of
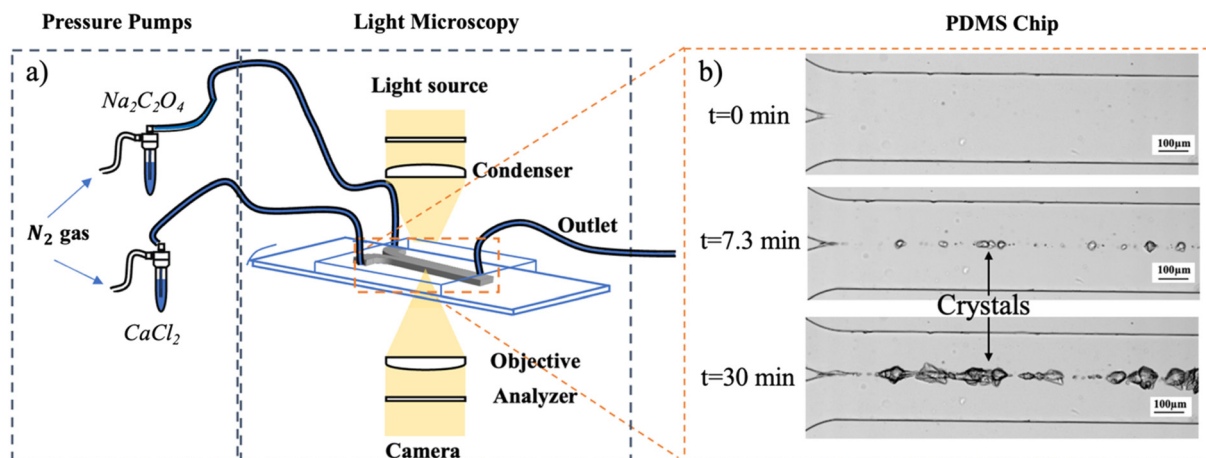
Fig. 1 a) The experimental setup with a microfluidic platform consisting of a pressure pump, a light source and a microscope with the chip. $CaCl_2$ and $Na_2C_2O_4$ were dissolved in artificial urine. b) The images were taken under the same experiment conditions (experiment AU4) at three time-lapses of 0, 7.3 and 30 minutes after the first crystal emerged.

water pumped through the system as a function of time. With known channel dimensions, the calculated volumetric flow rate was converted to mean flow velocities reported. The applied pressure difference of 25–85 dPa resulted in flow velocities of 0.015–0.075 m s^{-1}, respectively. Crystal growth was monitored using an automated optical microscope (Nikon Ti Series Inverted Microscope). One image was saved every 4 seconds for 30 minutes. The crystal growth at $t = 0$, $t = 7.3$, and $t = 30$ minutes for experiment AU4 is shown in Fig. 1b.

2.3. COMSOL model and JESS software

To rationalize the crystal growth of calcium oxalate qualitatively, the concentration gradients established due to the diffusion and convection in the laminar flow in the microchannel were calculated using COMSOL Multiphysics (see the ESI†). The calculated concentration profiles (considering 1.2, 1.6, 2.0 and 2.4 mol m^{-3} $Na_2C_2O_4$ at fixed 12 mol m^{-3} $CaCl_2$) in the channel were then used to calculate the relative supersaturation (σ) (Table 2) profiles in artificial urine values using Joint Expert Speciation System (JESS) software (see the ESI†). Since OPN and creatinine were not

included in the JESS database, these compounds were not considered in the supersaturation profile estimation.

2.4. Calculation method for the crystal growth rate

The image analysis tool Cellprofiler was used to analyze crystal areas using crystal images from the experiments. This detection was repeated for consecutive images with a time step of 40 seconds for 7.3 minutes starting at the emergence of the first crystal. This period for the growth rate calculation was chosen to avoid interferences in growth rate calculations by agglomeration in the channels observed at later stages in the experiments. An equivalent spherical shape was considered to calculate the radial growth of CaOx crystals. The measured 2D surface area (A) of about five crystals was converted to average radial size (r_{avg}) using eqn (1).

$$r_{avg} = \sqrt{(A/\pi)} \qquad (1)$$

To calculate the average growth rate ($\dot{r}_{avg}$), a linear fit was used regarding the average radial size (r_{avg}) and time step. In total, 11 data points are considered for each experimental condition during 7.3 minutes observation time.

2.5. Solution preparation with artificial urine

Artificial urine solution was prepared following the procedure reported by Streit et al.[40] (see Table 1). The ingredients (Table 1) were dissolved in ultrapure water using an ultrasonic probe to prepare artificial urine. $CaCl_2$ and $Na_2C_2O_4$ were added and dissolved in artificial urine in separate beakers just before the experiments and sent to the microchannel via two different inlets. The $CaCl_2$ and $Na_2C_2O_4$ concentrations added to fresh artificial urine are seen in Table 2.

Three main conditions, varying velocity, the molar ratio of Ca : Ox, in other words, supersaturation (σ) (in Table 2),

Table 1 Ingredients of artificial urine[40]

Compounds	Molarity [mM]	Source
Sodium chloride (NaCl)	90	Fluka
Potassium chloride (KCl)	42	Emsure
Ammonium chloride (NH$_4$Cl)	20	Sigma-Aldrich
Creatinine (C$_4$H$_7$N$_3$O)	7	Sigma-Aldrich
Urea (CH$_4$N$_2$O)	300	Emprove
Trisodium citrate (Na$_3$C$_6$H$_5$O$_7$)	2	Emprove
Magnesium sulphate heptahydrate (MgSO$_4$·7H$_2$O)	2	Sigma-Aldrich
Sodium sulphate (NaSO$_4$)	13	Sigma-Aldrich
Monobasic sodium phosphate (NaH$_2$PO$_4$)	16	Sigma-Aldrich

Table 2 Overview of added concentrations of CaCl$_2$ and Na$_2$C$_2$O$_4$ to artificial urine. Supersaturation (σ) values are determined using the JESS model. The latter values are only accurate until the point of nucleation

Experiment name	Molar ratio Ca : Ox	Added CaCl$_2$ [mol m^{-3}]	Added NaC$_2$O$_4$ [mol m^{-3}]	U [m s^{-1}]	σ values for COM from JESS	σ values for COD from JESS
AU1	7.5	12	1.6	0.015	46.8	17.8
AU2				0.035		
AU3				0.075		
AU4	5		2.4	0.035	67.6	26.3
AU5	6		2.0		57.5	21.9
AU6	10		1.2		34.7	13.5

Table 3 Overview of added concentrations of OPN to artificial urine at 12 mol m^{-3} CaCl$_2$ and 1.6 mol m^{-3} Na$_2$C$_2$O$_4$ with U = 0.015 m s^{-1}. OPN is dissolved in the Na$_2$C$_2$O$_4$ inlet and meets CaCl$_2$ in the channel

Experiment name	Molar ratio Ca : Ox	Added CaCl$_2$ [mol m^{-3}]	Added NaC$_2$O$_4$ [mol m^{-3}]	Added OPN [10^{-8} mol m^{-3}]	U [m s^{-1}]
AU7	7.5	12	1.6	2.4	0.015
AU8				6.0	
AU9				8.4	

and addition of OPN (Table 3), were tested in nine different experiments in artificial urine (AU) at room temperature.

It is noteworthy that the concentration of calcium was kept constant and higher than the other ions throughout all the experiments, in an effort to resemble the hypercalciuria
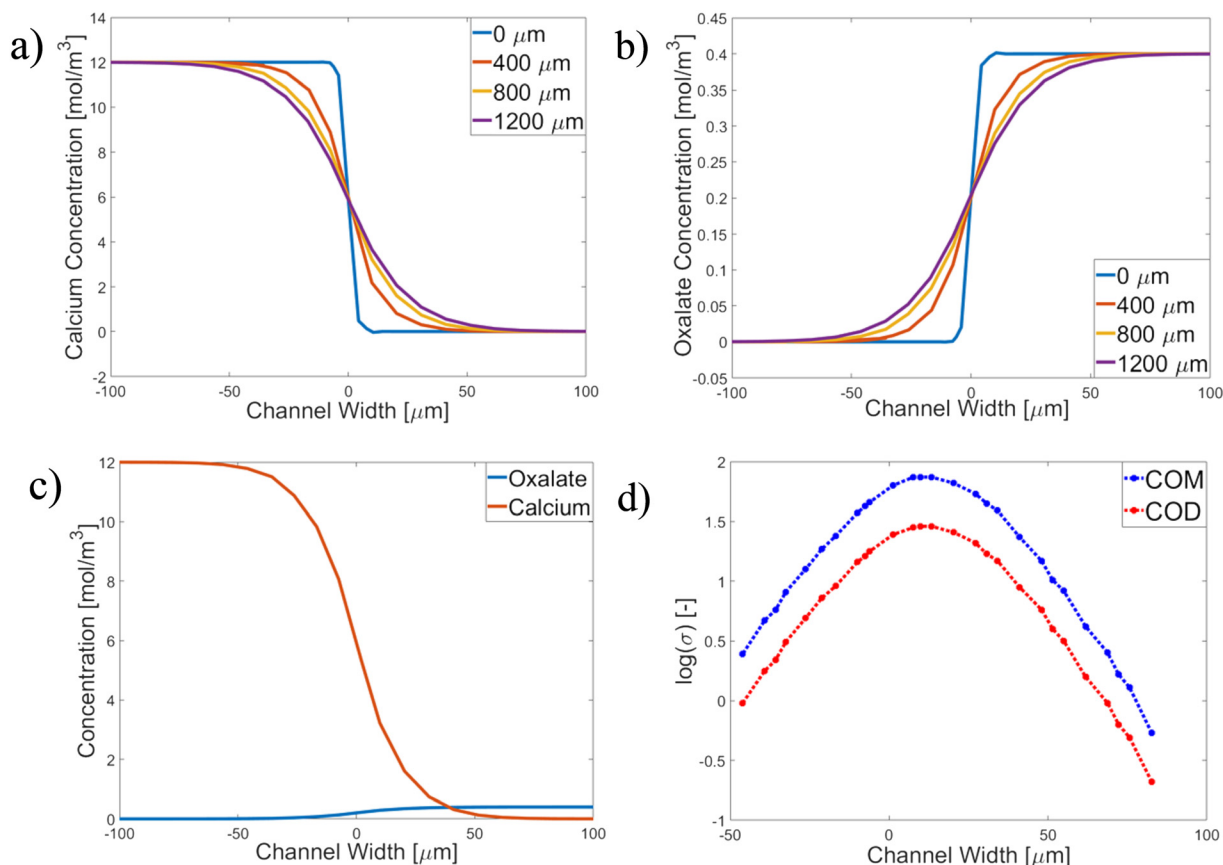
Fig. 2 Calcium and oxalate concentration profiles and σ-profile of experiment AU3 ([Ca^{2+}] = 12 mol m^{-3} and [Ox^{2-}] = 1.6 mol m^{-3} at U = 0.075 m s^{-1}, see Table 3) at the bottom of the channel with (a) concentration profiles of Ca^{2+} at different length positions (along the microchannel); (b) concentration profiles of Ox^{2-} at different length positions; (c) concentration profiles of Ca^{2+} (red) and Ox^{2-} (blue) at x = 800 μm (see Fig. S3 in the ESI†) considering that Ca^{2+} was fed at the right inlet (negative width region) and Ox^{2-} at the upper inlet (positive width region) (experiment AU3). (d) Logarithmic σ-profiles along the channel width for both COM and COD at x = 8000 μm.

condition in kidney stone patients – high Ca levels in the urine – while different flow velocities simulate urine flows – low urine flows reportedly increase kidney stone occurrence.[14,16,41–43]

3. Results and discussion

The growth rates ($\dot{r}_{avg}$) of both COM & COD crystals in artificial urine were determined under nine different conditions (Fig. 2–4). The concentrations of calcium and oxalate ions were estimated as a function of the position in the channel using COMSOL. The supersaturation profiles (σ) of COM and COD were calculated using these concentration profiles in JESS. As the crystals settled in the channel, the growth rates of individual crystals could be determined.

Summarized in Table 4 are the values for the flow velocity, the concentration of OPN, and the estimated relative supersaturation (σ) using JESS in the different experiments, along with the determined values of the average growth rates at t = 7.3 min.

3.1. Calculation of the supersaturation profile in the microscopy experiments using COMSOL and JESS

Calcium and oxalate concentration and supersaturation profiles through the channel were simulated using COMSOL. Fig. 2 shows the results for experiment AU3 (see Table 3 for the conditions). Fig. 2a and b show the concentration profiles in the channel. Because fixed crystals were observed on the bottom of the channel wall, c- and σ-profiles are shown at the channel bottom (z = 0 µm) at various length positions. The profiles at different positions change and become smoother further down the length of the channel due to diffusion of the Ca and Ox ions (see the ESI†). Fig. 2c shows the concentration profile at x = 800 µm for the ratio of Ca : Ox = 7.5 (experiment AU3) and Fig. 2d displays the logarithmic supersaturation σ-profiles with respect to COM and COD *vs.* the channel width at x = 800 µm (length) and z = 0 µm (depth) (the detailed COMSOL method is described in the ESI,† sections S2 and S3). The maximum supersaturation

values for COM and COD are seen at $y \sim 2$ µm (width) as $\log(\sigma_{COM})$ = 1.67 (σ = 46.8) and $\log(\sigma_{COD})$ = 1.25 (σ = 17.8).

The analysis of σ-profiles is done for all length positions and plotted in Fig. 3 after σ calculation with JESS using COMSOL concentration profiles (for details, see the ESI†). The supersaturation for COM is between the red lines, and for COD between the blue lines, while the maximum values of the supersaturation are close to the central dashed line in Fig. 3 (purple dots). Fig. 3 shows the results of experiment AU2 at 7.3 min after the first crystal was observed. The σ-profile is superimposed on the microscopy image of AU2. The trend of the σ-profile from COMSOL overlaps with the measured result. AU2 has 12 mol m^{-3} calcium and 1.6 mol m^{-3} oxalate with a molar ratio of 7.5 at a velocity value of 0.035 m s^{-1}. The difference in the concentration of the ions plays a role in the ion diffusion rate.

Fig. 3 shows that the small difference in ion concentrations allows effective diffusion of the oxalate ions into the calcium-rich side and σ_{max} is reached at $\approx$ 2 µm in the oxalate-rich side. The crystals (experiment AU2) emerged and grew at the interface, near the center of the channel, which overlaps with the COMSOL result.

3.2. Effect of average flow velocity on CaOx crystallization

To investigate the effect of flow velocity on the growth of the CaOx crystals, artificial urine experiments (AU1, AU2 and AU3) were performed with different velocities of 0.015, 0.035, 0.075 m s^{-1} at a fixed supersaturation value of COD of 17.8. The choice of flow speed range studied was based on reported flow rate values in the human collecting duct in the literature and experimental feasibility. First, we attempted to match the reported flow velocity in the collecting duct of the human kidneys (10 nl min^{-1} $\sim$ 0.0016 m s^{-1}),[32] which was not possible due to its very low value. Secondly, the maximum flow rate (0.075 m s^{-1}) was experimentally chosen considering the retention of the crystals in the microchannel – higher flow rates would drag the newly formed crystals out. Then, the lowest flow rate studied was selected so that the
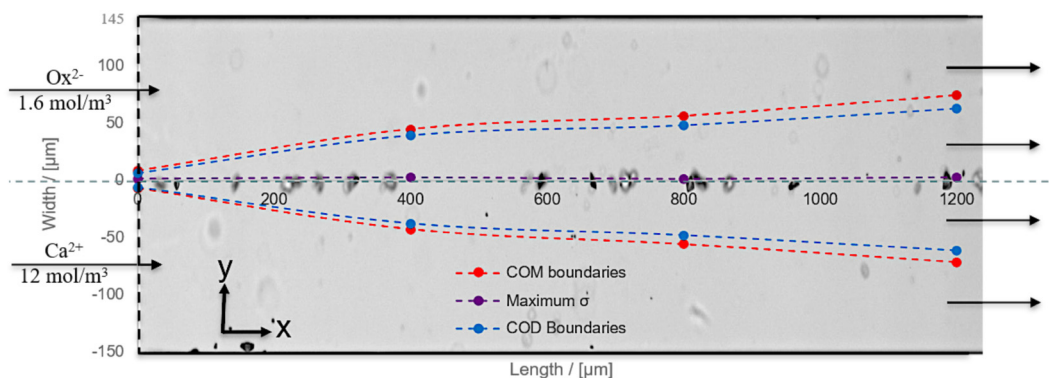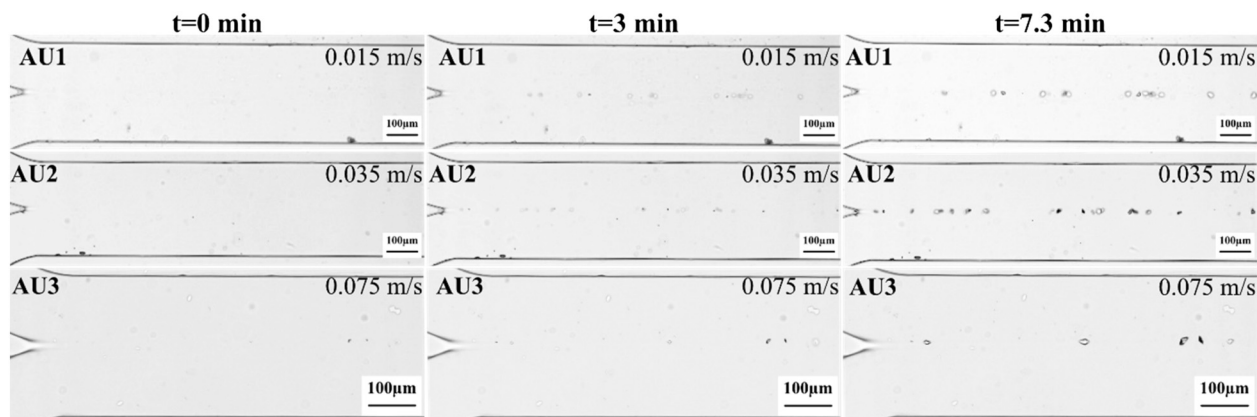

Fig. 3 COMSOL model combined with the image from artificial urine experiments at t = 7.3 min after the first observed crystal. Display of the situation for artificial urine experiment AU2 (see Fig. 4) with its experimental image.

Fig. 4 Microscopy images of the microfluidic channel for three experiments AU1, AU2 and AU3 (different rows) for varying flow velocities at 0.015, 0.035 and 0.075 m s^{-1}, respectively, at a fixed Ca : Ox molar ratio of 7.5. Time lapses of 0, 3 and 7.3 minutes after the first appearance of crystals (in columns) with a 10× objective, except for AU3 (with a 20× objective) with a 100 μm scale bar.

Table 4 Flow conditions, supersaturation and growth rates $\dot{r}_{avg}$ of COM and COD crystals in artificial urine at a fixed calcium concentration of 12 mol m^{-3}. The Ca : Ox ratio, flow velocity (U), added amount of OPN, supersaturation ratio values (σ) from JESS and growth rate ($\dot{r}_{avg}$) are shown. The presence of OPN was not taken into account in the calculation of supersaturation

Experimental conditions				COM			COD		
Experiment name	Molar ratio of Ca : Ox	U [m s^{-1}]	OPN [10^{-8} mol m^{-3}]	σ [–]	$\dot{r}_{avg}$ [10^{-8} m s^{-1}]	Std dev. [10^{-8} m s^{-1}]	σ [–]	$\dot{r}_{avg}$ [10^{-8} m s^{-1}]	Std dev. [10^{-8} m s^{-1}]
AU1	7.5	0.015	—	46.8	—	—	17.8	0.95	0.27
AU2	7.5	0.035	—	46.8	—	—	17.8	0.93	0.45
AU3	7.5	0.075	—	46.8	—	—	17.8	0.92	0.22
AU4	5	0.035	—	67.6	0.48	0.27	26.3	3.05	0.43
AU5	6	0.035	—	57.5	0.50	0.28	21.9	2.33	0.12
AU6	10	0.035	—	34.7	—	—	13.5	0.78	0.31
AU7	7.5	0.015	2.4	46.8	—	—	17.8	0.34	0.15
AU8	7.5	0.015	6.0	46.8	—	—	17.8	—	—
AU9	7.5	0.015	8.4	46.8	—	—	17.8	—	—

experiments could be conducted within reasonably accessible timescales in our laboratory. The maximum flow rate (0.075 m s^{-1}) was experimentally chosen considering the retention of the crystals in the microchannel – higher flow rates would drag the newly formed crystals out. Then, the lower flow rates were arbitrarily selected to investigate the effect of the flow rates on CaOx crystal growth, in an effort to understand the effect of low urine fluxes on kidney stone growth. Fig. 4 shows micrographs of the microfluidic channels at different times during the experiment. On the left side, the two inlet channels and their junction, where the CaCl$_2$ and Na$_2$C$_2$O$_4$ solutions meet, can be visualized, as detailed previously (Fig. 1). Crystals exhibiting tetragonal shapes were observed in the middle of the channel, which coincides with the interface between the two flows. In this work, crystals formed in the channels typically showed either tetragonal or oval shapes. In further analysis to identify the polymorphs, the spectrum for a tetragonal crystal revealed Raman shifts at 910 and 1474–1478 cm^{-1} (ref. 44–47) compatible with COD, while oval crystals were identified as COM[33] (section 7, ESI†). Hence, only COD crystals were seen at the interface under this supersaturation value. The composition of artificial urine containing magnesium and other trace metals may be responsible for the stabilization of the COD form at these supersaturation values, favoring the formation of COD over COM.[48–50]

COD crystals were monitored in the channels for 7.3 min after the first crystal emerged for each channel. The average growth rates ($\dot{r}_{avg}$) of COD were estimated to be 0.95 ± 0.27 × 10^{-8} m s^{-1}, 0.93 ± 0.45 × 10^{-8} m s^{-1}, and 0.92 ± 0.22 × 10^{-8} m s^{-1} with flow velocities of 0.015, 0.035, and 0.075 m s^{-1}, respectively (Table 4). The results showed that varying the flow velocity did not significantly affect the average growth rate ($\dot{r}_{avg}$), possibly due to the low Reynolds number (Re = 6.7 at the maximum velocity of 0.075 m s^{-1}). Since the flow from both inlets is laminar and co-current (x-axis), there is no influence in the diffusion of the ions from one stream to the other (y-axis); hence, the growth rates remain unaffected regardless of the flow velocities. Additionally, according to the COMSOL simulations (Fig. S4†), σ-profiles along the channel surface are not influenced significantly by varying U in the applied order of magnitude. The transport-

reaction kinetics for crystal growth are limited by the reaction, such that an increase in mass transport towards the surface would not lead to faster crystal growth. Hence, even if crystals grow large enough to reach parts of the channel where the fluid flow is highly convective, the growth rate is not expected to vary, since the system is reaction limited. Moreover, crystal growth occurs at the solid–liquid interface, where v = 0 m s^{-1}, so diffusion governs mass transfer.

3.3. The effect of the Ca : Ox molar ratio on CaOx crystallization

Fig. 5 shows the experiments performed with different oxalate concentrations at a fixed calcium (12 mol m^{-3}) concentration. The molar ratios of Ca : Ox in the experiments were 5, 6, 7.5, and 10 for AU4, AU5, AU2 and AU6, respectively. AU2 and AU6 resulted in the lowest values of supersaturation for COD: 17.8 and 13.5 and for COM: 46.8

and 34.7, respectively. In the experiments AU4 and AU5 with values of supersaturation COD: 26.3 and 21.9 and COM: 67.6 and 57.5, respectively, both crystal shapes, identified as COD and COM crystals were observed together. Our results using artificial urine are in line with Daudon $et\ al.$[51] results on patients' urine samples. These authors worked on 6869 urine samples with COM and COD crystals together. They reported that patients with higher Ca : Ox ratios (>14) excreted predominantly COD crystals, while patients with low Ca : Ox ratios (<5) excreted mostly COM. For the Ca : Ox ratios between these values, COM and COD were more equally distributed.

An example of how the average crystal growth rate of COM and COD is calculated is shown in Fig. 5C. The average size of five crystals (two COD and three COM crystals) was plotted as a function of time in Fig. 5C – as an example of the measurements conducted under various conditions studied. The slope of the linear fit to the data provides the average growth rate under given conditions. The estimation of the
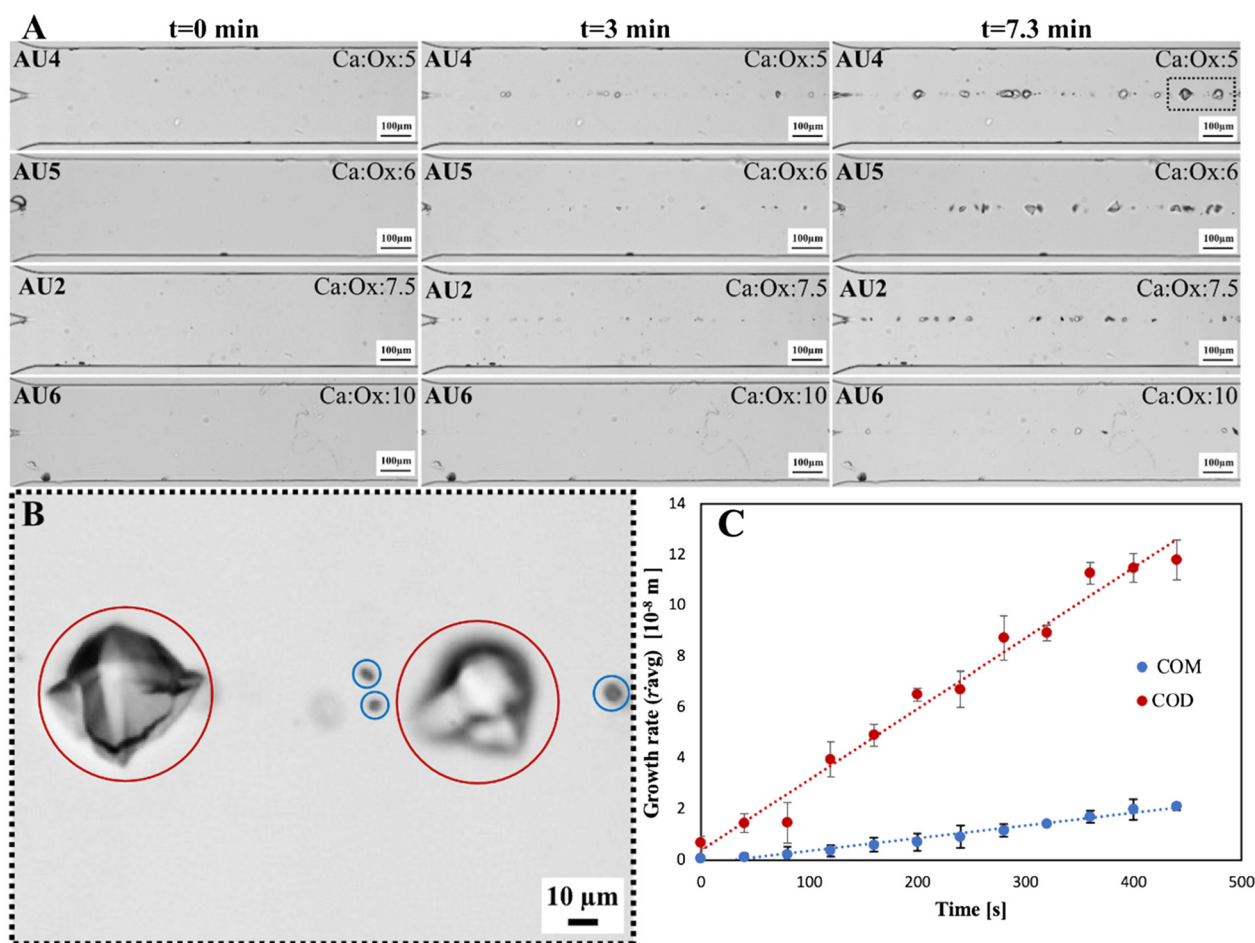
Fig. 5 A) Microscopy images of the microfluidic channel for four experiments AU4, AU5, AU2 and AU6 (different rows) for molar ratios of Ca : Ox of 5, 6, 7.5 and 10 at a fixed flow velocity of 0.035 m s^{-1}. Three time-lapses are shown after the first appearance of crystals (in columns) monitored with a 10× objective. B) The zoomed-in image of sample AU4 at t = 7.3 min visible in figure A in the black rectangle emphasizes the difference in growth rates between COM and COD crystals, circled blue and red, respectively (it is noteworthy that the crystals are blurred, which can be attributed to the difficulty in focusing due to different crystal heights – more images can be seen in the ESI,† Fig. S8). C) The average radius of three COM and two COD crystals (example sample) as a function of time from experiment AU4. The equation for COM is $\dot{r}_{avg}$ = 0.0048 t + 1.124 with its standard deviation, 0.0027 μm s^{-1}. The equation for COD is $\dot{r}_{avg}$ = 0.0305 t + 2.109 with its standard deviation, 0.0043 μm s^{-1}.

growth rate in each experiment was later generalized in a larger sample set for each experiment. The growth rate of the COD crystals showed strong dependence on the supersaturation, as can be seen in Table 4, and is the lowest at the highest Ca:Ox molar ratio of 10 in sample AU6. Surprisingly, the growth rates of the COM crystals did not vary significantly for the Ca:Ox ratio of 5 and 6, the highest supersaturation within these experiments.

3.4. Effect of osteopontin on CaOx crystallization

Fig. 6 shows the formation and growth of CaOx crystals as a function of OPN concentrations of 2.4×10^{-8} mol m^{-3}, 6.0×10^{-8} mol m^{-3} and 8.4×10^{-8} mol m^{-3} at a fixed Ca:Ox molar ratio of 7.5 and flow velocity of 0.015 m s^{-1}. It is noteworthy that AU1, shown in Fig. 4, can be used as a control experiment for the effect of OPN on the growth of CaOx crystals, since it was conducted under the same flow and Ca:Ox molar ratio conditions. The growth rate calculation was done using the images taken up until $t = 7.3$ min after the first crystal emerged, as for all the other conditions. To clarify the inhibition effect of OPN and show small COD crystals clearly, the images at $t = 30$ min are added in Fig. 6.

Contrary to what was observed in AU1 (Fig. 4), where COM crystals were observed up to 7.3 min, when OPN was added, the formation of a few COD crystals was only observed with the lowest OPN concentration of 2.4×10^{-8} mol m^{-3} for sample AU7 (Fig. 6). The higher OPN concentrations of 6.0×10^{-8} mol m^{-3} and 8.4×10^{-8} mol m^{-3} in AU8 and AU9 showed no CaOx crystal formation in artificial urine up until 30 min of observation. Thus, within this time, the nucleation was inhibited. To see the effect of the lowest OPN concentration, experiment AU7 should be compared with the control experiment, AU1, which has the same values of molar ratio and velocity (see Fig. 4 and Table 4). The growth rate of COD decreased from $0.95 \pm 0.27 \times 10^{-8}$ m s^{-1} (AU1) to $0.34 \pm 0.15 \times 10^{-8}$ m s^{-1} (AU7).

Studies in the literature claim that OPN can inhibit crystal growth and change the morphology of CaOx crystals.[52–54] Moreover, the chemical structure of OPN, rich in dicarboxylic acid groups, might encourage binding to a mineral surface,[52] thus a stronger interaction of OPN with CaOx crystal faces is likely to hinder crystal growth.[55]

The dual modulatory role of OPN has been discussed in the literature,[26] thus it is noteworthy to discuss it here. As shown in this study, *in vitro* experiments indicate that OPN inhibits the growth of CaOx crystals within the observation window. Yet, in the kidneys, the presence of OPN may trigger cell differentiation, mast cell degranulation and release of inflammatory mediators promoting stone formation. Moreover, the presence of competing ions such as phosphate[32] has been overlooked. Our results clearly do not include the OPN–kidney cell interactions, therefore this should be considered as a physiochemical model study.

As our experiments focus only on growth of crystals nucleated on PDMS chip walls, we rationalize that these crystals nucleated *via* heterogeneous nucleation. Homogeneous nucleation can still occur in the solution yet our experimental setup does not allow us to observe homogeneous nucleation occurring in solution. Regarding the role of aggregation particularly in the presence of OPN[26] and homogeneous nucleation in measured growth rates, the design of our experiments does not allow us to observe the growth of crystals nucleating in bulk *via* homogeneous nucleation and their aggregation. In other words, the observed growth rates are only extracted from crystals nucleated on the wall that are multiple crystal diameters away from each other.

4. Conclusion

We report the growth rates of CaOx crystals in artificial urine, in a geometry mimicking the collecting duct of the kidneys, under flow conditions relevant to kidney stone formation. The effect of varying flow velocities, the molar ratio of Ca:Ox, *i.e.*, distinct supersaturation, and OPN concentrations on the growth of CaOx crystals was investigated. Mainly COD crystals were observed in the channels. Altering the flow velocity in the channel did not affect crystal growth at a fixed supersaturation ratio.
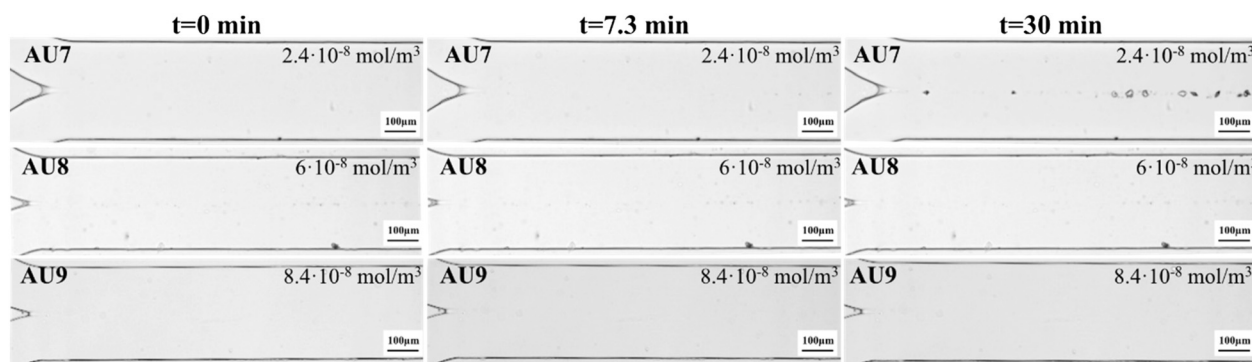
Fig. 6 Microscopy images of the microfluidic channel for experiments AU7, AU8 and AU9 (different rows) with different amounts of OPN; 2.4×10^{-8} mol m^{-3}, 6.0×10^{-8} mol m^{-3} and 8.4×10^{-8} mol m^{-3}, respectively, at a fixed Ca:Ox molar ratio of 7.5 and a flow velocity of 0.015 m s^{-1}. Three time lapses after the first appearance of crystals (in columns) with a 10× objective with a 100 μm scale bar.

However, an increase in the oxalate concentration at a fixed value of the Ca concentration (decreasing the Ca : Ox molar ratio, hence increasing the supersaturation at a fixed flow velocity) resulted in a clear increase in the average growth rate of COD crystals. In addition, for the lower molar ratios of calcium and oxalate (5 and 6), COM nucleation was also observed competing with the COD nucleation. The growth rate of the COM crystals did not show a clear dependence on the estimated supersaturation and was much lower than the COD growth rates. The presence of the lowest amount (*i.e.* 2.4×10^{-8} mol m^{-3}) of OPN in artificial urine decreased the growth rate of the COD crystals. With increasing OPN concentration, it was found that OPN inhibits crystal formation for both pseudopolymorphs of CaOx in artificial urine within the studied timeframe. This study focuses only on the physiochemical aspects of CaOx crystallization under flow conditions ignoring the dynamic effects arising from cellular interactions ever present in the kidneys. Therefore, we hope our study inspires future studies where the complexity of cell interactions in the kidneys is incorporated in microfluidic environments mimicking the kidneys.

Data availability

The authors confirm that the data supporting the findings of this study are available within the article and its ESI.† Any extra data that support the findings of this study are available from the corresponding author upon reasonable request.

Conflicts of interest

There are no conflicts to declare.

References

1 J. A. Wesson, R. J. Johnson, M. Mazzali, A. M. Beshensky, S. Stietz, C. Giachelli, L. Liaw, C. E. Alpers, W. G. Couser, J. G. Kleinman and J. Hughes, Osteopontin is a critical inhibitor of calcium oxalate crystal formation and retention in renal tubules, *J. Am. Soc. Nephrol.*, 2003, **14**(1), 139–147.

2 V. Romero, H. Akpinar and D. G. Assimos, Kidney stones: a global picture of prevalence, incidence, and associated risk factors, *Rev. Urol.*, 2010, **12**(2–3), e86–e96.

3 T. Alelign and B. Petros, Kidney Stone Disease: An Update on Current Concepts, *Adv. Urol.*, 2018, 3068365.

4 W. Wang, J. Fan, G. Huang, J. Li, X. Zhu, Y. Tian and L. Su, Prevalence of kidney stones in mainland China: A systematic review, *Sci. Rep.*, 2017, **7**(1), 41630.

5 I. Ogobuiro and F. Tuma, *Physiology renal*, StatPearls - NCBI Bookshelf, 2020.

6 H. W. Smith, *The kidney: structure and function in health and disease*, Oxford University Press, USA, 1951, vol. 1.

7 M. K. Bruce and A. S. Bruce, *Renal physiology*, Elsevier Mosby, Philadelphia, PA, 2013, p. 79.

8 G. Laffite, C. Leroy, C. Bonhomme, L. Bonhomme-Coury, E. Letavernier, M. Daudon, V. Frochot, J. P. Haymann, S. L. Rouzière, T. Ivan, D. Bazin, F. Babonneau and A. Abou-Hassan, Calcium oxalate precipitation by diffusion using laminar microfluidics: toward a biomimetic model of pathological microcalcifications, *Lab Chip*, 2016, **16**(7), 1157–1160.

9 P. D. Vize, A. S. Woolf and J. B. L. Bard, *The kidney: from normal development to congenital disease*, 2003, vol. 42.

10 P. Tabeling, *Introduction to microfluidics*, OUP Oxford, 2005.

11 J. E. Hall and M. E. Hall, *Guyton and Hall textbook of medical physiology e-Book*, Elsevier Health Sciences, 2020.

12 A. Asmar, P. K. Cramon, L. Simonsen, M. Asmar, C. M. Sorensen, S. Madsbad, C. Moro, B. Hartmann, B. L. Jensen, J. J. Holst and J. Bulow, Extracellular Fluid Volume Expansion Uncovers a Natriuretic Action of GLP-1: A Functional GLP-1-Renal Axis in Man, *J. Clin. Endocrinol. Metab.*, 2019, **104**(7), 2509–2519.

13 G. Bihl and A. Meyers, Recurrent renal stone disease—advances in pathogenesis and clinical management, *Lancet*, 2001, **358**(9282), 651–656.

14 F. L. Coe, M. J. Favus, C. Y. C. Pak, J. H. Parks, G. M. Preminger and D. A. Tolley, Kidney stones: Medical and surgical management, *Br. J. Urol.*, 1996, **78**(3), 482.

15 T. M. Reynolds, Best Practice No 181: Chemical pathology clinical investigation and management of nephrolithiasis, *J. Clin. Pathol.*, 2005, **58**(2), 134–140.

16 E. M. Worcester and F. L. Coe, Nephrolithiasis, *Prim. Care*, 2008, **35**(2), 369–391, vii.

17 K. Skorecki, G. M. Chertow, P. A. Marsden, M. W. Taal, S. L. Alan and V. Luyckx, *Brenner and Rector's The Kidney E-Book*, Elsevier Health Sciences, 2015.

18 C. Conti, M. Casati, C. Colombo, E. Possenti, M. Realini, G. D. Gatta, M. Merlini, L. Brambilla and G. Zerbi, Synthesis of calcium oxalate trihydrate: New data by vibrational spectroscopy and synchrotron X-ray diffraction, *Spectrochim. Acta, Part A*, 2015, **150**, 721–730.

19 V. Y. Bird and S. R. Khan, How do stones form? Is unification of theories on stone formation possible?, *Arch. Esp. Urol.*, 2017, **70**(1), 12.

20 X. Y. Sun, C. Y. Zhang, P. Bhadja and J. M. Ouyang, Preparation, properties, formation mechanisms, and cytotoxicity of calcium oxalate monohydrate with various morphologies, *CrystEngComm*, 2018, **20**(1), 75–87.

21 E. A. Boadi, S. Shin, F. Gombedza and B. C. Bandyopadhyay, Differential biomolecular recognition by synthetic vs. biologically-derived components in the stone-forming process using 3D microfluidics, *J. Mater. Chem. B*, 2022, **10**(1), 34–46.

22 V. N. Ratkalkar and J. G. Kleinman, Mechanisms of stone formation, *Clin. Rev. Bone Miner. Metab.*, 2011, **9**(3–4), 187–197.

23 K. P. Aggarwal, S. Narula, M. Kakkar and C. Tandon, Nephrolithiasis: Molecular Mechanism of Renal Stone Formation and the Critical Role Played by Modulators, *BioMed Res. Int.*, 2013, **2013**, 292953.

24 S. R. Qiu, A. Wierzbicki, C. A. Orme, A. M. Cody, J. R. Hoyer, G. H. Nancollas, S. Zepeda and J. J. De Yoreo, Molecular modulation of calcium oxalate crystallization by osteopontin

and citrate, *Proc. Natl. Acad. Sci. U. S. A.*, 2004, **101**(7), 1811–1815.

25 D. T. Denhardt, *Osteopontin: Role in Cell Signalling and Adhesion*, New York Academy of Sciences, 1995.

26 P. Peerapen and V. Thongboonkerd, Kidney stone prevention, *Adv. Nutr.*, 2023, **14**(3), 555–569.

27 H. Fleisch, Inhibitors and promoters of stone formation, *Kidney Int.*, 1978, **13**(5), 361–371.

28 P. Brown, D. Ackerman and B. Finlayson, Calcium oxalate dihydrate (weddellite) precipitation, *J. Cryst. Growth*, 1989, **98**(3), 285–292.

29 D. S. Ipe, E. Horton and G. C. Ulett, The Basics of Bacteriuria: Strategies of Microbes for Persistence in Urine, *Front. Cell. Infect. Microbiol.*, 2016, **6**, 14.

30 P. Mitra, D. K. Pal and M. Das, Does quality of drinking water matter in kidney stone disease: A study in West Bengal, India, *Investig. Clin. Urol.*, 2018, **59**(3), 158–165.

31 X. Geng, R. D. Sosa, M. A. Reynolds, J. C. Conrad and J. D. Rimer, Alginate as a green inhibitor of barite nucleation and crystal growth, *Mol. Syst. Des. Eng.*, 2021(7), 508–519.

32 F. Gombedza, S. Evans, S. Shin, E. Awuah Boadi, Q. Zhang, Z. Nie and B. C. Bandyopadhyay, Melamine promotes calcium crystal formation in three-dimensional microfluidic device, *Sci. Rep.*, 2019, **9**(1), 875.

33 F. Ibis, M. A. Nuhu, F. M. Penha, T. W. Yu, A. E. D. M. van der Heijden, H. J. M. Kramer and H. B. Eral, Role of Hyaluronic Acid on the Nucleation Kinetics of Calcium Oxalate Hydrates in Artificial Urine Quantified with Droplet Microfluidics, *Cryst. Growth Des.*, 2022, **22**(6), 3834–3844.

34 F. Ibis, Kidney stone in a chip: Understanding calcium oxalate kidney stone formation, TU Delft, 2022.

35 F. Ibis, T. W. Yu, F. M. Penha, D. Ganguly, M. A. Nuhu, A. E. D. M. van der Heijden, H. J. M. Kramer and H. B. Eral, Nucleation kinetics of calcium oxalate monohydrate as a function of pH, magnesium, and osteopontin concentration quantified with droplet microfluidics, *Biomicrofluidics*, 2021, **15**(2021), 1–17.

36 W. G. Robertson, Do "inhibitors of crystallisation" play any role in the prevention of kidney stones? A critique, *Urolithiasis*, 2017, **45**(1), 43–56.

37 P. Laval, J.-B. Salmon and M. Joanicot, A microfluidic device for investigating crystal nucleation kinetics, *J. Cryst. Growth*, 2007, **303**(2), 622–628.

38 R. M. Tona, T. A. O. McDonald, N. Akhavein, J. D. Larkin and D. Lai, Microfluidic droplet liquid reactors for active pharmaceutical ingredient crystallization by diffusion controlled solvent extraction, *Lab Chip*, 2019, **19**(12), 2127–2137.

39 S. Li, J. Ihli, W. J. Marchant, M. Zeng, L. Chen, K. Wehbe, G. Cinque, O. Cespedes, N. Kapur and F. C. Meldrum, Synchrotron FTIR mapping of mineralization in a microfluidic device, *Lab Chip*, 2017, **17**(9), 1616–1624.

40 J. Streit, L. Tran-Ho and E. Königsberger, Solubility of the three calcium oxalate hydrates in sodium chloride solutionsand urine-like liquors, *Monatsh. Chem.*, 1998, **129**(12), 1225–1236.

41 D. J. Kok and S. E. Papapoulos, Physicochemical considerations in the development and prevention of calcium oxalate urolithiasis, *Bone Miner.*, 1993, **20**(1), 1–15.

42 D. A. Bushinsky, J. R. Asplin, M. D. Grynpas, A. P. Evan, W. R. Parker, K. M. Alexander and F. L. Coe, Calcium oxalate stone formation in genetic hypercalciuric stone-forming rats, *Kidney Int.*, 2002, **61**(3), 975–987.

43 V. N. Ratkalkar and J. G. Kleinman, Mechanisms of Stone Formation, *Clin. Rev. Bone Miner. Metab.*, 2011, **9**(3–4), 187–197.

44 K. Rakotozandriny, S. Bourg, P. Papp, Á. Tóth, D. Horváth, I. T. Lucas, F. Babonneau, C. Bonhomme and A. Abou-Hassan, Investigating CaOx Crystal Formation in the Absence and Presence of Polyphenols under Microfluidic Conditions in Relation with Nephrolithiasis, *Cryst. Growth Des.*, 2020, **20**(12), 7683–7693.

45 C. A. Kuliasha, D. Rodriguez, A. Lovett and L. B. Gower, In situ flow cell platform for examining calcium oxalate and calcium phosphate crystallization on films of basement membrane extract in the presence of urinary 'inhibitors', *CrystEngComm*, 2020, **22**(8), 1448–1458.

46 V. Castiglione, P. Y. Sacre, E. Cavalier, P. Hubert, R. Gadisseur and E. Ziemons, Raman chemical imaging, a new tool in kidney stone structure analysis: Case-study and comparison to Fourier Transform Infrared spectroscopy, *PLoS One*, 2018, **13**(8), 1–18.

47 H. G. Edwards, M. R. Seaward, S. J. Attwood, S. J. Little, L. F. de Oliveira and M. Tretiach, FT-Raman spectroscopy of lichens on dolomitic rocks: an assessment of metal oxalate formation, *Analyst*, 2003, **128**(10), 1218–1221.

48 X. Martin, L. H. Smith and P. G. Werness, Calcium oxalate dihydrate formation in urine, *Kidney Int.*, 1984, **25**(6), 948–952.

49 R. Walton, J. Kavanagh, B. Heywood and P. Rao, The association of different urinary proteins with calcium oxalate hydromorphs. Evidence for non-specific interactions, *Biochim. Biophys. Acta, Gen. Subj.*, 2005, **1723**(1–3), 175–183.

50 B. Tomazic and G. Nancollas, The kinetics of dissolution of calcium oxalate hydrates, *J. Cryst. Growth*, 1979, **46**(3), 355–361.

51 M. Daudon, E. Letavernier, V. Frochot, J.-P. Haymann, D. Bazin and P. Jungers, Respective influence of calcium and oxalate urine concentration on the formation of calcium oxalate monohydrate or dihydrate crystals, *C. R. Chim.*, 2016, **19**(11–12), 1504–1513.

52 S. Qiu, A. Wierzbicki, C. Orme, A. Cody, J. Hoyer, G. Nancollas, S. Zepeda and J. De Yoreo, Molecular modulation of calcium oxalate crystallization by osteopontin and citrate, *Proc. Natl. Acad. Sci. U. S. A.*, 2004, **101**(7), 1811–1815.

53 D. T. Denhardt, *Osteopontin: role in cell signalling and adhesion*, New York Academy of Sciences, 1995.

54 J. A. Wesson, R. J. Johnson, M. Mazzali, A. M. Beshensky, S. Stietz, C. Giachelli, L. Liaw, C. E. Alpers, W. G. Couser, J. G. Kleinman and J. Hughes, Osteopontin is a critical inhibitor of calcium oxalate crystal formation and retention in renal tubules, *J. Am. Soc. Nephrol.*, 2003, **14**(1), 139–147.

55 L. Addadi and S. Weiner, Interactions between acidic proteins and crystals: stereochemical requirements in biomineralization, *Proc. Natl. Acad. Sci. U. S. A.*, 1985, **82**(12), 4110–4114.